Pergamon

Int. J. Solids Structures Vol. 34, No. 2, pp. 223–241, 1997

0020–7683/97 $15.00 + .00

0020–7683(95)00295–2

A LAMINATED SHELL MODEL FOR THE INFARCTED LEFT VENTRICLE

LARRY A. TABER and W. WILLIAM PODSZUS
Department of Mechanical Engineering, University of Rochester, Rochester, NY 14627, U.S.A.

(*Received* 30 *March* 1995; *in revised form* 15 *November* 1995)

Abstract—Experimental studies have shown that a region of partial dysfunction occurs in non-infarcted heart muscle near the edge of a myocardial infarction, where both blood flow and contractile function are compromised. Most data also indicate that the "border zone" for flow is much narrower than that for function. The factors responsible for these effects, which may lead to further infarction or other complications, are not completely understood. Thus, to study the mechanics of this problem, we present an ellipsoidal shell model for the infarcted left ventricle. The analysis of the model is based on a nonlinear shell theory that includes the effects of large axisymmetric deformation (with torsion), thick-shell effects, anisotropy, muscle activation, and residual stress. The governing equations are solved with a modified integrating matrix technique. We study both acute and chronic apical infarcts, which are represented by relatively soft and hard passive regions, respectively. Comparing theoretical and experimental pressure–volume relations and wall strains indicates that the model describes the mechanical behavior of the normal and ischemic left ventricle reasonably well. The model predicts significantly elevated end-systolic stresses inside an acute infarct, which may contribute to the complication of infarct expansion. Near the edge of the infarct, the results show that a relatively narrow bending boundary layer occurs within a much wider membrane boundary layer, suggesting that these layers correspond to the perfusion and functional border zones, respectively. The stiffer chronic infarct alleviates the stress concentrations in the border zone. Thus, treatment strategies should consider the relative differences in properties between the infarcted and noninfarcted regions. Copyright © 1996 Elsevier Science Ltd.

NOTATION

b = transverse shear factor ($=5/3$)
c_α = in-plane curvature measures
C_i = material constants
e_{ij} = Lagrange strains relative to reference configuration
E_w, $\bar{E}_w$ = wall thickening, normalized wall thickening
g_z = transverse shear strains
h = one-half shell thickness
H_z = horizontal stress resultants
I = strain invariant
$k_{\alpha\beta}$ = curvatures
K = number of laminae in shell
$M_{\alpha\beta}$ = moment resultants
n = transverse coordinate
$N_{\alpha\beta}$ = force resultants
p = internal pressure
p_H = horizontal pressure component
P = point on reference surface
P_z = moment resultant about normal to reference surface
q_i = applied surface moments
Q_α = transverse shear stress resultants
r = radial coordinate
$\bar{R}_1$, $\bar{R}_2$ = semimajor, semiminor shell axes
s = meridional coordinate
S = reference surface
S_z = transverse normal stress resultants
T_z = twisting moment
V = ventricular cavity volume
V_α = vertical stress resultants
w = two-dimensional strain-energy density function
W = three-dimensional strain-energy density function
x_i = shell coordinates

$\mathbf{y}$ = solution vector
z = axial coordinate
$\boldsymbol{\alpha}$ = shift tensor
β = fiber angle
γ_α = transverse shear strains
Γ_z, Γ_θ = transverse shear angles
δ_{ij} = two-dimensional Kronecker delta
ε_{ij} = Lagrange strains relative to end diastole
θ = circumferential coordinate
$\kappa_{z\beta}$ = curvature change measures
$\lambda_{z\beta}$ = two-dimensional stretch components
Λ_{ij} = three-dimensional stretch components
Λ_f = fiber stretch ratio
μ_α = shifters
σ_f, σ_c = fiber, cross-fiber Cauchy stresses
ϕ = meridional angle
ψ_α = in-plane curvature changes
ω = circumferential rotation angle of point on reference surface
Ω = circumferential rotation angle of shell face.

1. INTRODUCTION

A myocardial infarction ("heart attack") is a region of oxygen-starved (ischemic) heart muscle that becomes necrotic. Most infarcts occur in the left ventricle (LV) and are produced by occlusion of a coronary artery, with the blockage due most often to a fractured atherosclerotic plaque or a thrombus (blood clot). Myocardial infarctions also can be precipitated by an imbalance between oxygen supply and demand, without total obstruction of an artery. Wall stresses can affect both sides of the supply-demand equation. Elevated wall stresses increase oxygen consumption by increasing energy requirements (Sarnoff *et al.*, 1958; Skelton and Sonnenblick, 1974; Sagawa *et al.*, 1988) and can limit oxygen supply by compressing intramyocardial vessels, particularly during systolic contraction (Downey *et al.*, 1974; Hoffman *et al.*, 1985).

Abnormal wall stresses also may contribute to the complications that follow myocardial infarction, which include infarct expansion, extension, and rupture (Weisman and Healy, 1987). Infarct expansion is a permanent dilatation of the infarcted region, while infarct extension involves additional necrosis in the region immediately adjacent to the original infarction. Many expanded infarcts eventually become ventricular aneurysms, which are permanent outpocketings of the wall composed of mature scar tissue. Rupture of the wall most often occurs during the first few weeks post-infarction, before the healing process is completed. All of these complications can severely reduce life expectancy.

An issue that has been debated for several years is whether a border zone (BZ) of moderately ischemic myocardium surrounds an infarct. If such a zone exists, it likely predisposes the region to infarct extension. Appropriate treatment, on the other hand, may be able to salvage the ischemic tissue (Braunwald and Maroko, 1974). Mechanically, a boundary layer would be expected to occur at the edge of an infarct, and experimental results support the presence of a *functional border zone* (FBZ), where contraction is compromised (Sakai *et al.*, 1985; Gallagher *et al.*, 1987a, b; Nanto *et al.*, 1993). However, most recent data indicate that the transition region from the unperfused infarct to the normally perfused myocardium, the *perfusion border zone* (PBZ), is much narrower than the FBZ (Hirzel *et al.*, 1977; Murdock *et al.*, 1983; Sakai *et al.*, 1985; Gallagher *et al.*, 1987a, b). Here again, wall stress may be an important factor.

The purpose of the present study is to examine the stresses predicted by a model for the infarcted LV. The model is a laminated, ellipsoidal shell of revolution that includes the effects of large deformation, anisotropy, and muscle contraction. Both acute (relatively soft) and chronic (relatively stiff) apical infarcts are studied. The results suggest that membrane stresses dominate contractile dysfunction, while bending stresses dominate intramyocardial blood-flow impediment. Thus, therapy aimed to alter local stress distributions, not only peak wall stress, may be warranted.

2. MODEL

To a first approximation, the LV is a thick-walled ellipsoidal shell (Fig. 1a). The myocardial fibers wind around the ventricular cavity and, relative to the circumferential direction, change orientation angle across the wall from about 60° at the endocardium to −60° at the epicardium (Streeter, 1979). The fibers are bound by a highly ordered interstitial collagen matrix (Caulfield and Borg, 1979).

Representing the basic structure, our model for the LV is an ellipsoidal shell of revolution (Fig. 1a) composed of pseudoelastic, incompressible laminae that are transversely isotropic relative to the local fiber direction. The fiber angle β is constant across each layer but varies piecewise linearly across the wall from 60° to −60°. For the canine LV in the reference (unloaded passive) state, we use the representative dimensions $\bar{R}_1 = 2.39$ cm and $\bar{R}_2 = 1.09$ cm, respectively, for the inner semimajor and semiminor axes of the shell (Fig. 1a). In addition, the base of the LV is located above the equator by $\bar{R}_1/2$, and the wall thickness $2\bar{h}$ is 0.60 cm. The base is taken clamped to a rigid end plate representing the mitral valve ring, while the remainder of the shell is allowed to translate and rotate freely. The shell is subjected only to a specified internal pressure p, and all of the results contain the effects of residual strain for a circumferential opening angle of 30° [see Taber (1991a)].

Transmural infarcts are studied by modifying the material properties of a specified axisymmetric region at the apex. During the healing process, the necrotic muscle tissue is replaced gradually by fibrous scar tissue. Experimental measurements indicate that the stiffness of infarcted myocardium increases significantly within the first few hours following infarction, reaches a peak in the first couple of weeks, and then decreases (Parmley *et al.*, 1973; Gupta *et al.*, 1994). A fibrous infarct, however, remains at least five times stiffer than normal myocardium. In this work, we examine two limiting cases: acute infarcts, representing the first few minutes post-infarction, and chronic infarcts, representing several weeks or months after infarction. Acute infarcts are modeled as myocardium that remains passive during the cardiac cycle, with the passive properties remaining normal; chronic

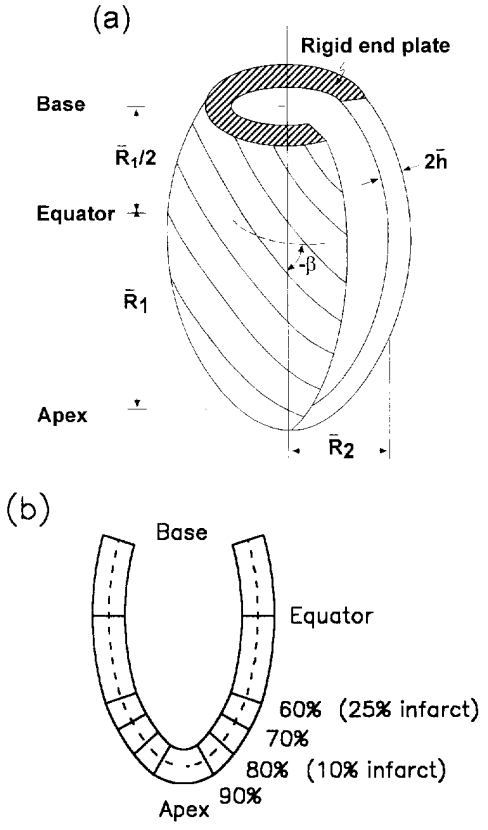

Fig. 1. (a) Model of left ventricle. (b) Meridional locations.

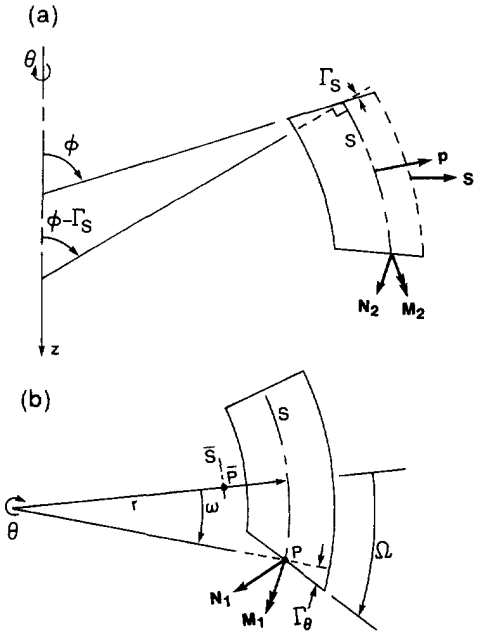

Fig. 2. Side view (a) and top view (b) of differential shell element.

infarcts are modeled as inextensible caps, with geometries fixed by the unloaded passive configuration of the normal LV.† Outside the infarcted region in both cases, the myocardium is assumed to have normal contractile properties.

Results are presented for a model composed of nine layers of equal thickness. We examine the normal LV and the LV with apical transmural infarcts occupying 10% and 25% of the LV reference surface area (approximately 6% and 15% of the wall volume). These infarcts involve the lower 20% and 40%, respectively, of the shell meridian (Fig. 1b). Here, we focus on the behavior at end diastole (ED) and end systole (ES).

3. ANALYSIS

The analysis of the model is based on our previously published theory for relatively thick shells composed of incompressible muscle (Taber, 1991b). This theory accounts for the effects of anisotropy, geometric and material nonlinearities, transverse shear deformation, and transverse normal stress and strain. Muscle activation and residual stress are handled through shifts in the local zero-stress state for a shell element. The present study uses equations specialized for the case of axisymmetric deformation of shells of revolution with axial torsion. (The anisotropy induces torsion.) A similar analysis for cylindrical geometry was presented by Taber (1991a).

Consider an ellipsoidal shell of revolution with axis of symmetry $\bar{z}$ (Fig. 1a). For convenience, we refer to the unloaded passive configuration as the "undeformed" configuration, even though residual stresses may be present. Relative to a global polar coordinate system, the coordinates of a point $\bar{P}$ on the undeformed reference surface $\bar{S}$ are $(\bar{r}, \bar{\theta}, \bar{z})$. An arbitrary point in the undeformed wall is located by the "shell" coordinates $(\bar{\theta}, \bar{s}, \bar{n}) \equiv (\bar{x}_1, \bar{x}_2, \bar{x}_3)$, where $\bar{s}$ is the meridional and $\bar{n}$ the transverse normal direction along the reference surface, and the geometry of $\bar{S}$ is defined by a relation of the form $\bar{r} = \bar{r}(\bar{s})$. Note that bars indicate the *undeformed* state.

Deformation carries the point $\bar{P}(\bar{r}, \bar{\theta}, \bar{z})$ on $\bar{S}$ to the point $P(r, \theta, z)$ on the deformed reference surface S. Lines normal to $\bar{S}$ and S enclose the angles $\bar{\phi}$ and $\phi - \Gamma_s$, respectively, with the axis of symmetry, where ϕ is the meridional angle of the deformed *face* of a shell element (Fig. 2a). Similarly, due to torsion, the circumferential face rotates through an

†Recently, Gupta *et al.* (1994) published biaxial data on the mechanical properties of infarcts. Unfortunately, these data did not become available until our study was complete.

angle Ω about the $\bar{z}$-axis, with $\omega = \Omega - \Gamma_\theta$ being the circumferential angle between P and $\bar{P}$ (Fig. 2b). The angles Γ_s and Γ_θ are measures of the transverse shear deformation.

3.1. *Shell equations*

Here, we list the governing equations of the theory; details of their derivation can be found in Taber (1988; 1991b). These relations describe the deformation relative to the unloaded passive (reference) configuration. Modifications to include muscle activation and residual stress are discussed later. Note that symbol definitions are listed under Notation, the subscripts (1, 2, 3) denote the $(\bar{\theta}, \bar{s}, \bar{n})$ directions, and prime denotes differentiation with respect to $\bar{s}$. In addition, stress and moment resultants are defined per unit undeformed length, Greek subscripts take the values 1 and 2, and Latin subscripts take the values 1, 2, 3. (The summation convention is *not* employed.)

Reference-surface strains:

$$\begin{aligned} e_{11} &= r\cos\Gamma_\theta/\bar{r} - 1, \quad e_{21} = r\omega'\cos\Gamma_\theta - r'\sin\Gamma_\theta, \\ e_{12} &= r\cos\phi\sin\Gamma_\theta/\bar{r}, \quad e_{22} = (r'\cos\Gamma_\theta + r\omega'\sin\Gamma_\theta)\cos\phi + z'\sin\phi - 1, \\ \gamma_1 &= r\sin\phi\sin\Gamma_\theta/\bar{r}, \quad \gamma_2 = (r'\cos\Gamma_\theta + r\omega'\sin\Gamma_\theta)\sin\phi - z'\cos\phi. \end{aligned} \tag{1}$$

Reference-surface stretches:

$$\begin{aligned} \lambda_{\alpha\beta} &= \delta_{\alpha\beta} + e_{\alpha\beta} \\ \lambda_{33} &= (\lambda_{11}\lambda_{22} - e_{12}e_{21})^{-1}. \end{aligned} \tag{2}$$

Curvature change measures:

$$\begin{aligned} \kappa_{\alpha\beta} &= \lambda_{33}k_{\alpha\beta} - \lambda_{\alpha\beta}\bar{k}_{\alpha\alpha} \\ \psi_\alpha &= c_\alpha - \bar{c}_\alpha \end{aligned} \tag{3}$$

$$\begin{aligned} &\bar{k}_{11} = \sin\bar{\phi}/\bar{r}, \quad \bar{k}_{12} = 0, \quad \bar{c}_1 = -\cos\bar{\phi}/\bar{r}, \\ &\bar{k}_{21} = 0, \quad \bar{k}_{22} = \bar{\phi}', \quad \bar{c}_2 = 0, \\ &k_{11} = \sin\phi/\bar{r}, \quad k_{12} = 0, \quad c_1 = -\cos\phi/\bar{r}, \\ &k_{21} = \Omega'\sin\phi, \quad k_{22} = \phi', \quad c_2 = -\Omega'\cos\phi. \end{aligned} \tag{4}$$

Horizontal and vertical stress resultants:

$$\begin{aligned} H_1 &= N_{12}\cos\phi + Q_1\sin\phi \\ H_2 &= N_{22}\cos\phi + Q_2\sin\phi \\ V_1 &= N_{12}\sin\phi - Q_1\cos\phi \\ V_2 &= N_{22}\sin\phi - Q_2\cos\phi. \end{aligned} \tag{5}$$

Force equilibrium:

$$\begin{aligned} (\bar{r}H_2)' &= N_{11} + \bar{r}\Omega' N_{21} - \bar{r}p_H \\ \bar{r}V_2 &= \frac{pr^2}{2}\left[1 - \frac{\lambda_{33}\bar{h}}{r}\right]^2 \\ T_z/2\pi &= (\bar{r}H_2)r\sin\Gamma_\theta + (\bar{r}N_{21})r\cos\Gamma_\theta + (\bar{r}M_{21})\sin\phi \\ &\quad + \int_0^{\bar{s}} [(\bar{r}p_H)r\sin\Gamma_\theta + (\bar{r}M_{11})k_{12}\sin\phi]\,\mathrm{d}\bar{s}. \end{aligned} \tag{6}$$

Moment equilibrium:

$$(\bar{r}M_{22})'/\bar{r}+c_1M_{11}+c_2M_{21}-\lambda_{22}Q_2-e_{12}Q_1+\gamma_1N_{12}+\gamma_2N_{22}-(k_{11}P_1+k_{21}P_2+q_1)=0$$

$$(\bar{r}M_{21})'/\bar{r}-c_1M_{12}-c_2M_{22}-\lambda_{11}Q_1-e_{21}Q_2+\gamma_1N_{11}+\gamma_2N_{21}+(k_{12}P_1+k_{22}P_2+q_2)=0$$

$$(\bar{r}P_2)'/\bar{r}+k_{11}M_{12}+k_{21}M_{22}-k_{12}M_{11}-k_{22}M_{21}+\lambda_{11}N_{12}-\lambda_{22}N_{21}$$
$$-e_{12}N_{11}+e_{21}N_{22}+q_3=0 \quad (7)$$

$$S_1=\lambda_{33}^{-1}(\lambda_{11}Q_1+e_{21}Q_2-\gamma_1N_{11}-\gamma_2N_{21})$$
$$S_2=\lambda_{33}^{-1}(\lambda_{22}Q_2+e_{12}Q_1-\gamma_1N_{12}-\gamma_2N_{22})$$
$$S_3=-\lambda_{33}^{-1}(k_{11}M_{11}+k_{12}M_{12}+k_{21}M_{21}+k_{22}M_{22}). \quad (8)$$

Constitutive relations:

$$N_{\alpha\beta}=\frac{\partial w}{\partial e_{\alpha\beta}},\quad Q_\alpha=b\frac{\partial w}{\partial\gamma_\alpha},\quad S_\alpha=b\frac{\partial w}{\partial g_\alpha},\quad M_{\alpha\beta}=\lambda_{33}\frac{\partial w}{\partial\kappa_{\alpha\beta}},\quad P_\alpha=\frac{\partial w}{\partial\psi_\alpha}. \quad (9)$$

The quantity p_H in eqns (6) is the horizontal component of the applied load per unit area of $\bar{S}$. For an internal pressure p,

$$p_H=\mu_1\,\mu_2\,p\lambda_{11}\lambda_{22}\sin(\phi-\Gamma_\alpha) \quad (10)$$

where

$$\mu_\alpha=1+nk_{\alpha\alpha}$$
$$\tan\Gamma_\alpha=\frac{r'\sin\phi-z'\cos\phi\cos(\Omega-\omega)}{r'\cos\phi+z'\sin\phi\cos(\Omega-\omega)}$$
$$\Gamma_\theta=\Omega-\omega \quad (11)$$

with $\mu_\alpha^-\equiv\mu_\alpha(-h)$. Finally, note that the strain measures are of the Biot type.

3.2. *Strain-energy function*

The constitutive relations (9) are written in terms of the two-dimensional strain-energy function w. For a shell composed of K laminae,

$$w=\sum_{k=1}^{K}\int_{n^{(k-1)}}^{n^{(k)}}W^{(k)}(\Lambda_{ij})\mu_1\mu_2\,\mathrm{d}\bar{n} \quad (12)$$

where $W^{(k)}$ is the three-dimensional strain-energy function per unit undeformed volume of layer k, and the $n^{(k)}$ define the transverse locations of the layer interfaces. The present work uses an expansion for w that includes the effects of incompressibility, residual strain, and muscle activation [see Taber (1991b) for details]. As outlined below, the latter two effects are included by modifying the zero-stress reference state for W.

Passive residual stress and muscle activation alter the local zero-stress configuration. Thus, for each material element, we introduce a passive and an active zero-stress state. The governing equations above are written relative to a reference state, which we choose as the unloaded passive state (including any passive residual stress). The deformation of the reference state relative to the passive zero-stress state is described by the deformation gradient tensor $\boldsymbol{\alpha}_P$, and the deformation of the passive zero-stress state relative to the active zero-stress state is described by the deformation gradient tensor $\boldsymbol{\alpha}_A$. The tensors $\boldsymbol{\alpha}_P$ and $\boldsymbol{\alpha}_A$ are determined *a priori* through appropriate experiments [see Taber (1991a)].

For the myocardium, we take

$$W = W_P + W_A \tag{13}$$

where W_P and W_A are passive and active strain-energy contributions, respectively. For the passive part in material coordinates, we use

$$W_P = C_1(\Lambda_{f_P} - 1)^2 + C_2(\Lambda_{f_P} - 1)^3 + C_3(I_P - 3) + C_4(I_P - 3)(\Lambda_{f_P} - 1) + C_5(I_P - 3)^2 \tag{14}$$

which Humphrey *et al.* (1990a, b) deduced from biaxial tensile tests. In this equation, Λ_{f_P} is the fiber stretch ratio and

$$I_P = (\Lambda_{11}^2 + \Lambda_{12}^2 + \Lambda_{13}^2 + \Lambda_{21}^2 + \Lambda_{22}^2 + \Lambda_{23}^2 + \Lambda_{31}^2 + \Lambda_{32}^2 + \Lambda_{33}^2)_P \tag{15}$$

is a strain invariant, where the three-dimensional stretches Λ_{f_P} and Λ_{i_P} are expressed relative to the passive zero-stress state (using α_P). Humphrey *et al.* (1990a) provided several sets of values for the material constants C_i from which we choose

$$C_1 = 20.98, \quad C_2 = 22.11, \quad C_3 = 2.45, \quad C_4 = -13.26, \quad C_5 = 11.34$$

where all parameters are in mm Hg. These values give a predicted end-diastolic pressure–volume relation (EDPVR) that is similar to a typical experimental curve for the normal canine LV (Fig. 3a).

The active strain-energy function is taken as (Taber, 1991a)

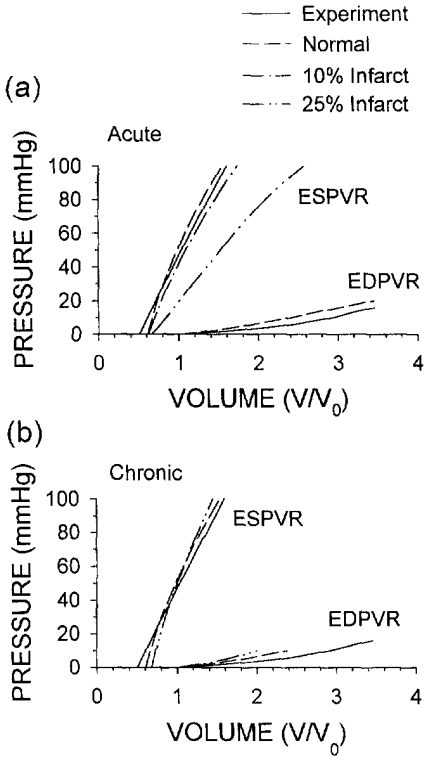

Fig. 3. End-diastolic (EDPVR) and end-systolic (ESPVR) pressure–volume relations for LV with acute infarct (a) and chronic infarct (b).

$$W_A = C_6(\Lambda_{f_A}^2 + \Lambda_{f_A}^{-2} - 2)^{C_7} \tag{16}$$

where the fiber stretch ratio Λ_{f_A} is computed relative to the active zero-stress state (using $\boldsymbol{\alpha}_P$ and $\boldsymbol{\alpha}_A$). During diastolic filling $C_6 = 0$, and empirically fitting the theoretical to the experimental end-systolic pressure–volume relation (ESPVR) for the normal canine LV gives $C_6 = 204$ mm Hg and $C_7 = 1.4$ at ES (Fig. 3a).

3.3. *Method of solution*

Equations (1), (3), (5), (6), (7), (8), and (9) constitute 38 equations in 38 unknowns.† r, z, ϕ, Ω, ω, $e_{\alpha\beta}$, γ_α, g_α, $\kappa_{\alpha\beta}$, ψ_α, $N_{\alpha\beta}$, Q_α, $M_{\alpha\beta}$, P_α, S_i, H_α, and V_α. The terms involving q_i and P_α in the moment equations contribute higher order effects due to moments turning about the n direction (Taber, 1988), and the curvature changes ψ_α do not appear in our second-order expansion for w. Thus, we neglect these unknowns and eliminate eqns $(3)_2$ and $(9)_5$, reducing the system to 34 equations and unknowns. The boundary conditions consist of zero displacement and rotation (of the meridional face) at the base and the symmetry conditions $\lambda_{11} = \lambda_{22}$ and $\kappa_{11} = \kappa_{22}$ at the apex.

The governing equations were solved numerically using an integrating matrix technique (Parnell, 1984), which we previously modified to accommodate a mixed system of nonlinear differential and algebraic equations (Kempski *et al.*, 1988; Podszus, 1992). As detailed in the appendix, the shell equations can be written in the form

$$\frac{d\mathbf{y}_D}{d\bar{s}} = \mathbf{b}_D(\mathbf{y})$$

$$0 = \mathbf{b}_A(\mathbf{y}) \tag{17}$$

where $\mathbf{b}_D$ and $\mathbf{b}_A$ are nonlinear functions of the solution vector

$$\mathbf{y} = [\mathbf{y}_D, \mathbf{y}_A]^T, \tag{18}$$

with $\mathbf{y}_D$ and $\mathbf{y}_A$ containing the differential and the algebraic dependent variables, respectively. The integrating matrix transforms eqn $(17)_1$ into a system of nonlinear algebraic difference equations, and then the full system of algebraic equations is solved using an implicit Newton-Raphson scheme [see Podszus (1992) for details].

4. PRESSURE–VOLUME RELATIONS

The pressure–volume behavior of the LV depends on the type and size of infarct (Fig. 3). Due to the assumption of unaltered passive properties in the infarcted region, the EDPVR of the acutely infarcted LV is unaffected (Fig. 3a). The ESPVR, however, shifts to the right relative to that of the normal LV, and its slope decreases as the infarct size increases. Correspondingly, while the ED profile of the acutely infarcted LV is the same as that of the normal LV, the 25% infarct (by reference-surface area) bulges considerably at ES (Fig. 4a). This paradoxical systole may lead to a permanent bulge, i.e., infarct expansion, through remodeling or plastic deformation.

For the chronic infarct, the diastolic stiffness of the LV increases (Fig. 3b), as the ED profile shows decreased cavity volume (Fig. 4b). The ES stiffness also increases but not as much as does the ED stiffness, as the ES profile is nearly normal (Fig. 4b). All of these results agree qualitatively with those of Bogen *et al.* (1980; 1984), who presented a spherical membrane model for the infarcted LV.

For the normal LV, we specified the typical ED and ES pressures of 10 and 100 mm Hg, respectively. For the 25% acutely infarcted ventricle, however, the volume at an ES pressure of 100 mm Hg is *greater* than the volume at an ED pressure of 10 mm Hg (Fig. 3a). Thus, the stroke volume would be negative unless ED volume is increased. Increasing

†The unknown κ_{12} and the constitutive relation for M_{12} are dropped [see Taber (1988)].

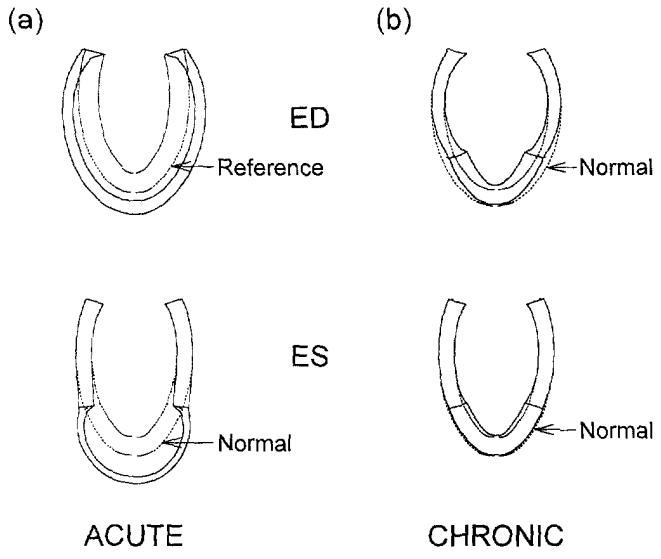

Fig. 4. Computed end-diastolic and end-systolic profiles of LV with acute infarct (a) and chronic infarct (b).

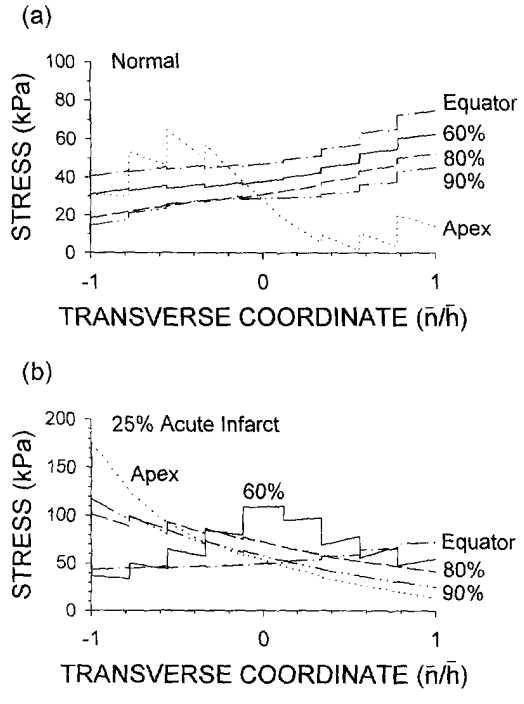

Fig. 5. End-systolic transmural Cauchy fiber stress distributions at several meridional locations in normal LV (a) and 25% acutely infarcted LV (b). The infarct in (b) is located between the 60% location and the apex. Note the different scales.

the ED pressure to 20 mm Hg produces a stroke volume similar to that of the normal ventricle. Thus, the results presented in the following sections for the 25% acutely infarcted ventricle are based on an ED pressure of 20 mm Hg.

5. STRESS DISTRIBUTIONS

5.1. *Normal ventricle*

Transmural distributions of Cauchy fiber stress† in the normal LV at ES are shown for several meridional locations (Fig. 5a). Away from the apex, the stress profiles at the

†For convenience, we refer to the total stress (matrix + fiber) in the fiber direction as the "fiber" stress.

various sections (equator to 80%, see Fig. 1b) are similar qualitatively and are like those published for anisotropic cylinder models (Arts *et al.*, 1979; Taber, 1991a). Near the apex, the location of the peak fiber stress shifts away from the epicardium, and a subendocardial stress concentration develops.

Thus, the subendocardial layers near the apex must sustain a greater load than most other regions of the normal LV, with a corresponding increase in contractile energy demand and oxygen consumption. These findings are consistent with the greater susceptibility of the subendocardial apical regional to ischemic insult and subsequent myocardial infarction (Schlichter *et al.*, 1954; Gorlin *et al.*, 1967). However, this region also may be more susceptible to compromised blood supply, since it is served last by the coronary arteries.

5.2. *Acute infarct*

The equatorial region sees little direct influence of the 25% acute infarct (compare Figs 5a, b). Near and inside the acutely infarcted myocardium ($\geqslant 60\%$), however, the ES transmural fiber stress distributions are altered significantly relative to those in the normal ventricle. At the infarct edge (60% location), the peak stress nearly doubles and shifts from the epicardium to midwall. Inside the infarct, the maximum stress occurs at the endocardium and, at the apex, almost triples the normal value. As shown by longitudinal distributions, the relative change in cross-fiber stress is even greater (Fig. 6a). These large stresses within the infarct may damage the collagen microstructure, leading to infarct expansion (Zhao *et al.*, 1987; Whittaker *et al.*, 1991). Note also that the infarct stresses in the fiber and cross-fiber directions are similar (Fig. 6), consistent with a nearly spherical bulge.

The longitudinal stress profiles show the details of the behavior in the BZ (Fig. 6). But first, to illustrate the basic ideas behind the following discussion, we consider a pressurized circular cylinder with a clamped edge (Fig. 7). A thin membrane (dashed curve) with negligible bending rigidity can satisfy a zero-displacement, but not a zero-slope, boundary condition. Far from the edge, the deformation is uniform. Near the edge, however, the zero-displacement condition forces the development of a "membrane" boundary layer (M) that widens as the pressure increases. For a shell (solid curve), the zero-slope condition induces a "bending" boundary layer (B) that narrows with increasing pressure [see Taber (1987a, b) for further discussion].

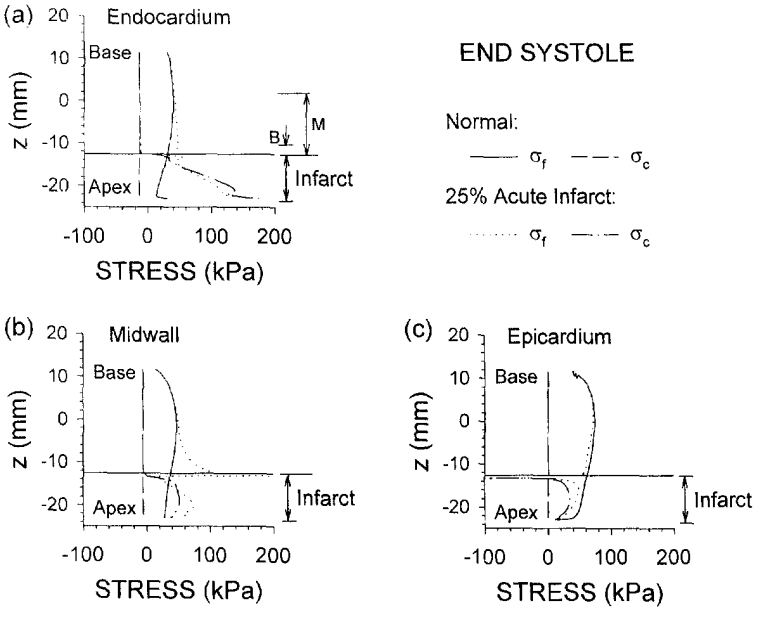

Fig. 6. End-systolic Cauchy stress distributions along meridian in normal and acutely infarcted LV: (a) endocardium; (b) midwall; (c) epicardium. (z = distance from equator; σ_f = fiber stress; σ_c = in-plane cross-fiber stress; M = membrane boundary layer; B = bending boundary layer.)

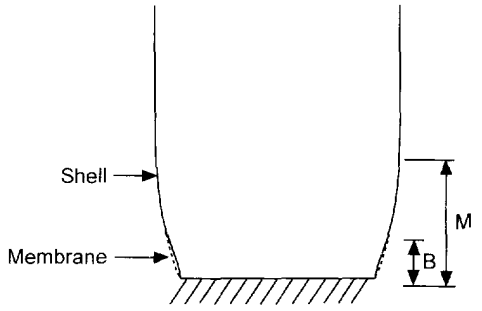

Fig. 7. Membrane (M) and bending (B) boundary layers near edge of clamped pressurized cylinder.

In the noninfarcted myocardium near the infarct edge, the fiber stress distributions reflect a similar type of boundary layer effect (Fig. 6). Since the infarct is flexible, however, the behavior differs in some respects, as the bulging infarct pulls the adjacent myocardium outward at ES. The membrane boundary layer (M) produces a stress increase near the infarct, in qualitative agreement with the results given by the membrane models of Bogen *et al.* (1980) and Needleman *et al.* (1983). The midwall fiber stress at the infarct edge is nearly triple the normal value (Fig. 6b). The narrower bending boundary layer (B) is characterized primarily by decreased fiber stress at the endocardium (Fig. 6a), as the bending rigidity prevents some of the outward tethering. This boundary layer has a much stronger effect near the epicardium just inside the infarct (Fig. 6c), where a local concentration of high compressive stress occurs.

These results suggest that the membrane boundary layer defines the relatively wide FBZ, and the bending boundary layer defines the narrower PBZ. Comparing Figs 6 and 4a at ES shows that the membrane layer corresponds approximately to the region of perturbed deformation. The bending layer can be seen in the deformed LV profile, but it is much less detectable. Our model predicts large epicardial compressive stresses due to bending just *inside* the infarct. If the systolic stiffness in the BZ is lessened, a similar effect also would occur just outside the infarct. The large compressive epicardial stresses may compress intramyocardial vessels, hampering flow from the surface arteries and providing the relatively narrow PBZ compared to the FBZ. The stress concentrations also may induce the larger cellular hypertrophy (Olivetti *et al.*, 1986) and the increased myocyte slippage due to collagen damage (Zhao *et al.*, 1987; Whittaker *et al.*, 1991) that occur in the BZ. The combined effects of decreased flow and increased oxygen consumption due to elevated ES stress also could explain in part, why second infarcts often occur at the edge of first infarcts (Schlichter *et al.*, 1954).

5.3. *Chronic infarct*

Since the ES configuration of the LV is similar to the reference configuration (Fig. 4b), the chronic infarct primarily affects the mechanics at ED. Due to strong bending, the greatest alteration in stress occurs near the infarct edge at the epicardium, where the peak stress in the infarcted LV is compressive and has a magnitude about eight times that in the normal LV (Fig. 8c). This extremely narrow boundary layer supports the lack of a significant PBZ after healing. (Note that perfusion of the subendocardial layers normally occurs during diastole.) Due to the relatively small ED pressure, however, these stresses remain smaller than the ES stresses (not shown). In addition, note that similarly large compressive stresses also are present at the base in both the normal and the infarcted ventricles. This is a consequence of the assumption that the base is clamped to the mitral valve ring.

6. COMPARISON TO EXPERIMENTAL RESULTS

A limited number of quantitative experimental studies are available for comparison. First, the computed wall thickening at ES is compared to the data of Gallagher *et al.* (1987b), who used sonomicrometers to measure the impairment in wall thickening across

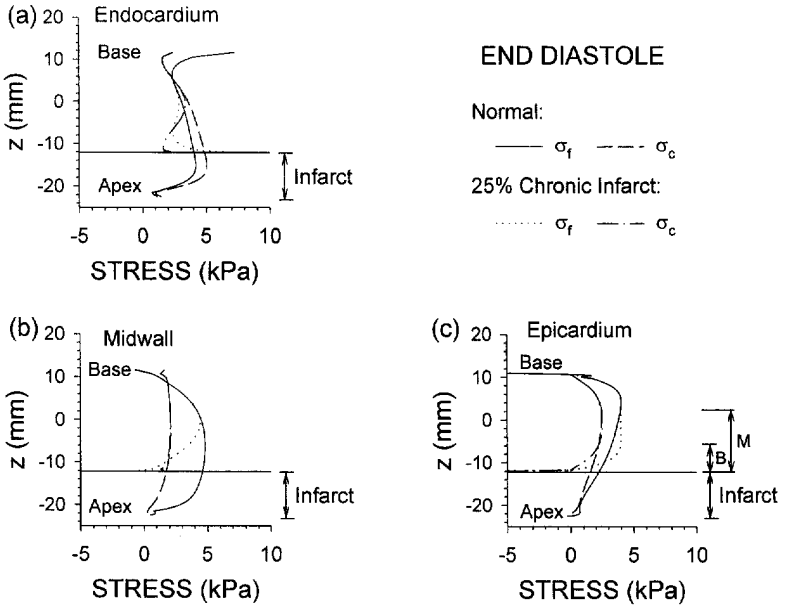

Fig. 8. End-diastolic Cauchy stress distributions along meridian in normal and chronically infarcted LV : (a) endocardium ; (b) midwall ; (c) epicardium. (z = distance from equator ; σ_f = = fiber stress ; σ_c = in-plane cross-fiber stress ; M = membrane boundary layer ; B = bending boundary layer.)

an ischemic boundary in the canine LV. With $2h_{ES}$ and $2h_{ED}$ being the ES and ED wall thickness, the wall thickening is defined as

$$E_w = h_{ES}/h_{ED} - 1, \tag{19}$$

and the normalized wall thickening at each location along the meridian is defined by

$$\bar{E}_w = (E_w)_{\text{infarct}}/(E_w)_{\text{normal}} \tag{20}$$

where $(E_w)_{\text{normal}}$ is measured before occlusion. Note that $(E_w)_{\text{normal}} > 0$ since the wall normally thickens during systole ; thus, $\bar{E}_w < 0$ indicates systolic thinning.

The 25% acute infarct model predicts the same general pattern of normalized wall thickening that the experimental preparation demonstrates (Fig. 9). Gallagher *et al.* (1987b) defined the FBZ as the distance from the ischemic boundary to 97.5% of the nonischemic asymptote of a fitted (dotted) curve. This criterion gives experimental and theoretical BZ widths of about 7.8 and 7.5 mm, respectively.

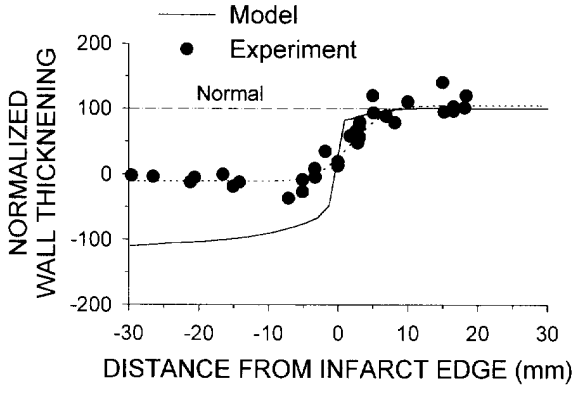

Fig. 9. Normalized wall thickening ($\bar{E}_w$) near edge of infarct. Experimental data are from Gallagher *et al.* (1987b).

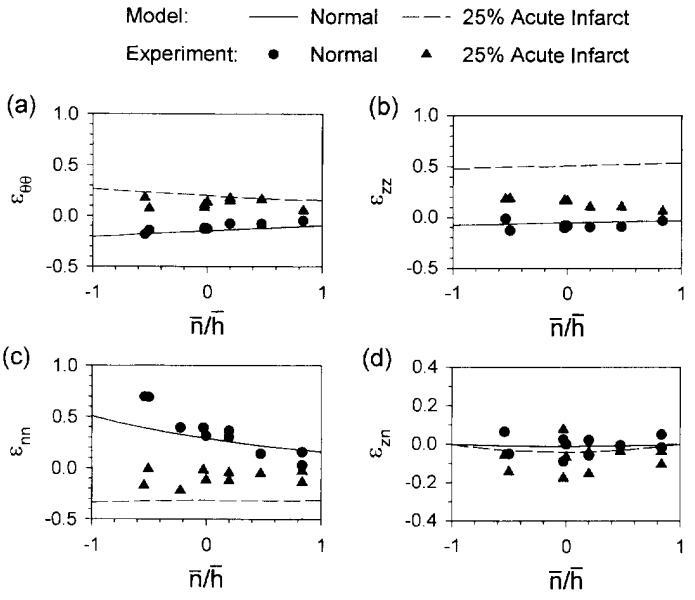

Fig. 10. End-systolic transmural Lagrange strain distributions relative to end diastolic configuration in normal LV and in acutely infarcted region (model) and ischemic region (experiment). Model results are for 70% location within a 25% infarct, and experimental data are from Villarreal *et al.* (1991).

There is, however, one notable difference between the experimental and theoretical results. The experimental results exhibit little thinning in the infarcted area (Fig. 9), but the model gives substantial thinning. This discrepancy may be due to residual contraction in the experimental ischemic myocardium. The size of the ischemic region also may be a factor. Unfortunately, Gallagher *et al.* (1987b) did not estimate the size of their ischemic area.

Villarreal *et al.* (1991) measured three-dimensional wall strains in the mid-anterior free wall of canine LVs before and after 10 min of induced transmural ischemia. The ED pressure approximately doubled between the normal and ischemic ventricles, consistent with our assumption (see Section 4). The 25% acute infarct model was used to compute end-systolic Lagrange strains (ε_{ij}) in shell coordinates relative to the ED configuration inside the 25% infarct at the 70% location (see Fig. 1b). Transmural strain distributions show relatively good agreement between the measured and computed normal strain components both before and after occlusion (Figs 10a, b, c). After occlusion, the shortening strains $\varepsilon_{\theta\theta}$ and ε_{zz} in the normal ventricle are replaced by lengthening strains, while the infarct thins ($\varepsilon_{nn} < 0$) rather than thickens during systole. The predicted changes in ε_{zz} and in the shear strain ε_{zn}, however, are too small. These discrepancies may be due to residual contraction in the ischemic myocardium. Nevertheless, considering the variability inherent in biological tissues and the uncertainty over whether the model parameters accurately reflect the experimental specimen, the relative agreement between the two sets of results is encouraging.

Recently, van Leuven *et al.* (1994) measured epicardial strains across the perfusion boundary in the pig heart following 90 minutes of induced regional ischemia. For the following reasons, however, comparing their data with our model predictions is of rather limited use. First, the experimental perfusion boundary was oriented primarily in a longitudinal direction, and so the strain distribution was measured in a predominantly circumferential direction. Our axisymmetric model assumes no circumferential variation. Second, similar to the results of Gallagher *et al.* (1987b), the ischemic region exhibited little systolic expansion. Third, the measured strain normal to the ischemic boundary was continuous across the boundary, in contradiction to the discontinuous meridional strain distributions predicted by the present acute infarct model and that of Bogen *et al.* (1980; 1984). The theoretical predictions are a consequence of the assumed sharp discontinuity in

material properties between the normal and infarcted regions. One possible explanation for the measured results is that the ischemic boundary actually consists of interdigitating perfused and nonperfused muscle.

7. DISCUSSION

Clinical and experimental evidence indicates a strong correlation between the level of wall stress and proper functioning of the heart. Wall stress influences intramyocardial blood flow, oxygen consumption, hypertrophy, and structural remodeling.

The results of the present investigation suggest three primary conclusions. First, the peak wall stresses within a large transmural acute infarct can nearly triple those in the normal LV. These stresses may damage the collagen matrix, leading to infarct expansion, aneurysm, or rupture (Zhao *et al.*, 1987; Whittaker *et al.*, 1991).

Second, two types of boundary layers alter the mechanics in the noninfarcted myocardium near the edge of an infarct. A relatively wide membrane boundary layer is associated with the FBZ, and a much narrower boundary layer is associated with the PBZ. Experimental studies have indicated that in-plane tensile stresses have little effect on coronary flow (Krams *et al.*, 1989; Resar *et al.*, 1992; Livingston *et al.*, 1993), but the large compressive stresses predicted by the model in the epicardial layers (Figs 6c and 8c) may cause arteries to constrict or collapse, preventing flow into the deeper layers. The elevated tensile fiber stresses (Fig. 6b), on the other hand, likely increase oxygen consumption. These effects may lead to infarct extension.

Third, stress concentrations near the edge of a chronic infarct generally are less severe than those near an acute infarct (Figs 6 and 8). Thus, the healing process may be driven, in part, by mechanisms that seek to lessen the workload in the BZ. This view is supported by the cellular hypertrophy than occurs in the BZ (Olivetti *et al.*, 1986).

7.1. *Border zone*

The presence of a FBZ surrounding a region of ischemic or infarcted myocardium apparently is accepted by most investigators. During acute ischemia in humans, dogs, and pigs, respectively, Nanto *et al.* (1993), Gallagher *et al.* (1987a, b), and Sakai *et al.* (1985) have measured FBZs about 10–15 mm wide, consistent with the width of the membrane boundary layer in our model (Fig. 6). Also consistent with the present model, authors have attributed this behavior to a tethering effect, with the decreased contraction of the ischemic area inhibiting the contraction of the adjacent noninfarcted myocardium.

In contrast, the presence of a PBZ of moderately ischemic tissue remains controversial. Some researchers describe transition zones from low to high perfusion as wide as 15 mm (Cox *et al.*, 1968; Hearse *et al.*, 1977; Prinzen *et al.*, 1989). Others find either a very narrow (< 3 mm) PBZ or none at all (Hirzel *et al.*, 1977; Murdock *et al.*, 1983; Sakai *et al.*, 1985; Gallagher *et al.*, 1987a, b). The discrepancies in these results may be due to differences in preparation and measurement techniques. The width of the bending boundary layer in our model (Fig. 6) is consistent with the concept of a very narrow PBZ about 3 mm wide.

7.2. *Other models*

Although many models have been proposed for the normal LV [see Yin (1981; 1985) and McCulloch *et al.* (1992) for reviews], there have been relatively few attempts to model the infarcted LV. Models of acute infarcts have focused generally on the effects of infarct size and thickness on rupture potential and global cardiac performance. The first model of the infarcted LV was presented by Lowe and Love (1948), who treated the infarct as a relatively soft bulge on a spherical ventricle. Using variations of this model, Mirsky *et al.* (1978) and Radhakrishnan *et al.* (1980) concluded that rupture potential depends more on the thickness of the infarct than on its size. Although these models provide useful information, they neglect the mechanical coupling between the infarcted and noninfarcted tissue.

Using a finite-element model, Janz and Waldron (1978) investigated the effects of chronic apical infarcts. Their finite-element model was based on an axisymmetric representation of the rat LV and accounted for large deformations, but the myocardium was

taken as isotropic. The model of Vinson *et al.* (1979) incorporated more realistic three-dimensional geometry and anisotropy, but nonlinear behavior and the transmural distribution in fiber angle were not considered. Both of these models examined only diastolic behavior.

In a series of papers, Bogen *et al.* (1980; 1984) and Needleman *et al.* (1983) presented a spherical isotropic membrane model that includes the effects of large deformation and muscle activation. To examine various post-infarction stages, they modeled apical infarcts as axisymmetric caps of various stiffnesses. The predicted EDPVRs compare favorably with those of Janz and Waldron (1978), illustrating that global behavior can be predicted by a thin-walled model. The computed ESPVRs for various size infarcts are consistent with experimental and clinical data. They also found elevated stresses and strains in the BZ adjacent to the infarct boundary, corresponding to the membrane boundary layer of the present model. The stress concentration depended strongly on the infarct stiffness and on contractility of the viable myocardium, wherein it decreased with the former and increased with the latter.

Membrane models are generally adequate for studying global behavior, but computing local stress concentrations requires the inclusion of thick-wall effects. Bovendeerd (1990) used a large-deformation, anisotropic, finite-element model to investigate diastolic and systolic behavior of the LV with an asymmetric transmural infarct. A rough estimate suggested that the FBZ, based on deformation, is about twice as wide as that for subepicardial blood flow, in agreement with the experimental results of Prinzen *et al.* (1989). However, their mesh was too coarse to examine the BZ behavior in detail.

7.3. *Limitations*

Our conclusions are subject to several limitations, which involve the geometry, the boundary conditions, the material properties, and the theoretical analysis. First, the geometry of the LV and the infarcted region is highly idealized. While an ellipsoid of revolution is a reasonable approximation for the LV (Streeter, 1979), including asymmetries yields more complex stress distributions (Vinson *et al.*, 1979; van Campen *et al.*, 1994). Moreover, although most infarcts involve the apex, they are not really axisymmetric. Including asymmetry would affect our results quantitatively, but the predicted behavior is probably correct qualitatively since the Gaussian curvature is positive through most of the undeformed LV.

The assumption of a clamped base is likely too constraining, but simple support is probably no more realistic. The predicted stresses near the mitral valve, therefore, may be too large. In addition, we neglected external loads due to the right ventricle and the pericardium. These effects should be examined in future work.

The constitutive behavior of passive and active myocardium is not yet completely understood. The passive strain-energy function used here [eqn (14)] is based on biaxial tests involving extension but not compression. Thus, the extremely large compressive stresses predicted by the model near the infarct edge (Figs 6c and 8c) may be suspect, although the qualitative behavior is correct. Furthermore, the models for the two limiting cases considered here, i.e., an infarct with normal passive properties and one with infinite stiffness, likely predict higher stresses than those which actually occur. The active strain-energy function also needs further experimental confirmation. (Note that contraction velocity does not affect ED and ES.) Improved accuracy awaits more complete data.

Finally, there is the question of applying shell theory to such a thick shell, which has a radius-to-thickness ratio of about 2 3. Our theory accounts for the thick-shell effects of transverse shear deformation and transverse normal stress, and Taber (1989; 1991a) has investigated the accuracy of this theory for shells as thick as the LV, finding surprising accuracy for simple geometries. On the other hand, the expansion for the 2-D strain-energy function is based on the assumption that the squares of the bending and transverse shear strains are small compared to unity (Taber, 1988, 1991b). Near the infarct edge, these strains exceed this restriction. Thus, a three-dimensional stress analysis is required in this region to compute accurate stresses.

Despite these limitations, the comparisons with experimental data (Figs 9 and 10) indicate that our model yields a reasonable description of the basic mechanics. More realistic features should be added in the future.

In conclusion, our shell model for the LV indicates that the mechanical behavior within and near an infarct may play a role in subsequent complications. Effective treatment likely depends not only on reducing overall workload, but also on reducing the differences in properties between the infarcted and noninfarcted myocardium.

Acknowledgements—The authors than Dr William B. Hood, Jr, of the University of Rochester School of Medicine for inspiring this work originally and for many useful discussions. This research was supported by NIH grant R01 HL46367 (L.A.T.). The supercomputer time granted from the John von Neumann National Supercomputer Center at Princeton University (grant NAC-22026) and from the National Center for Supercomputing Applications at the University of Illinois (grant CES-900003N) is also acknowledged.

REFERENCES

Arts, T., Reneman, R. S. and Veenstra, P. C. (1979). A model of the mechanics of the left ventricle. *Ann. Biomed. Engng* **7,** 299–318.

Bogen, D. K., Rabinowitz, S. A., Needleman, A., McMahon, T. A. and Abelmann, W. H. (1980). An analysis of the mechanical disadvantage of myocardial infarction in the canine left ventricle. *Circ. Res.* **47,** 728–741.

Bogen, D. K., Needleman, A. and McMahon, T. A. (1984). An analysis of myocardial infarction: the effect of regional changes in contractility. *Circ. Res.* **55,** 805–815.

Bovendeerd, P. H. M. (1990). The mechanics of the normal and ischemic left ventricle during the cardiac cycle: a numerical and experimental analysis. Ph.D. thesis, University of Limburg, Maastricht, The Netherlands.

Braunwald, E. and Maroko, P. R. (1974). The reduction of infarct size—an idea whose time (for testing) has come. *Circulation* **50,** 206–209.

Caulfield, J. B. and Borg, T. K. (1979). The collagen network of the heart. *Lab. Invest.* **40,** 364–372.

Cox, J. L., McLaughlin, V. W., Flowers, N. C. and Horan, L. G. (1968). The ischemic zone surrounding acute myocardial infarction. Its morphology as detected by dehydrogenase staining. *Am. Heart J.* **76,** 650–659.

Downey, J. M., Downey, H. F. and Kirk, E. S. (1974). Effects of myocardial strains on coronary blood flow. *Circ. Res.* **34,** 286–292.

Gallagher, K. P., Gerren, R. A., Choy, M., Stirling, M. C. and Dysko, R. C. (1987a). Subendocardial segment length shortening at lateral margins of ischemic myocardium in dogs. *Am. J. Physiol.* **253,** H826–H837.

Gallagher, K. P., Gerren, R. A., Ning, X. H., McManimon, S. P., Stirling, M. C., Shlafer, M. and Buda, A. J. (1987b). The functional border zone in conscious dogs. *Circulation* **76,** 929–942.

Gorlin, R., Klein, M. D. and Sullivan, J. M. (1967). Prospective correlative study of ventricular aneurysm. *Am. J. Med.* **42,** 512–531.

Gupta, K. B., Ratcliffe, M. B., Fallert, M. A., Edmunds, L. H. and Bogen, D. K. (1994). Changes in passive mechanical stiffness of myocardial tissue with aneurysm formation. *Circulation* **89,** 2315–2326.

Hearse, D. J., Opie, L. H. and Katzeff, I. E. (1977). Characterization of the border zone in acute regional ischemia in the dog. *Am. J. Cardiol.* **40,** 716–726.

Hirzel, H. O., Sonnenblick, E. H. and Kirk, E. S. (1977). Absence of a lateral border zone of intermediate creatine phosphokinase depletion surrounding a central infarct 24 hours after acute coronary occlusion in the dog. *Circ. Res.* **41,** 673–683.

Hoffman, J. I. E., Baer, R. W., Hanley, F. L. and Messina, L. M. (1985). Regulation of transmural myocardial blood flow. *J. Biomech. Engng* **107,** 2–9.

Humphrey, J. D., Strumpf, R. K. and Yin, F. C. P. (1990a). Determination of a constitutive relation for passive myocardium: II. Parameter estimation. *J. Biomech. Engng* **112,** 340–346.

Humphrey, J. D., Strumpf, R. K. and Yin, F. C. P. (1990b). Determination of a constitutive relation for passive myocardium I. A new functional form. *J. Biomech. Engng* **112,** 333–339.

Janz, R. F. and Waldron, R. J. (1978). Predicted effect of chronic apical aneurysms on the passive stiffness of the human left ventricle. *Circ. Res.* **42,** 255–263.

Kempski, M. H., Taber, L. A. and Su, F. C. (1988). Large elastic deformation of shear deformable shells of revolution: numerical and experimental results. *J. Appl. Mech.* **55,** 629–634.

Krams, R., Sipkema, P., Zegers, J. and Westerhof, N. (1989). Contractility is the main determinant of coronary systolic flow impediment. *Am. J. Physiol.* **257,** H1936–H1944.

Livingston, J. Z., Resar, J. R. and Yin, F. C. P. (1993). Effect of tetanic myocardial contraction on coronary pressure-flow relationships. *Am. J. Physiol.* **265,** H1215–H1226.

Lowe, T. E. and Love, E. R. (1948). Cardiac aneurysms: a mechanical analysis of their deformation. *Aust. J. Exp. Biol. Med. Sci.* **26,** 497–513.

McCulloch, A., Waldman, L. and Rogers, J. (1992). Large-scale finite element analysis of the beating heart. *CRC Crit. Rev. Biomed. Engng* **20,** 427–449.

Mirsky, I. McGill, P. L. and Janz, R. F. (1978). Mechanical behavior of ventricular aneurysms. *Bull. Math. Biophys.* **40,** 451–464.

Murdock, R. H., Harlan, D. M., Morris, J. J., Pryor, W. W. and Cobb, F. R. (1983). Transitional blood flow zones between ischemic and nonischemic myocardium in the awake dog: analysis based on distribution of the intramural vasculature. *Circ. Res.* **52,** 451–459.

Nanto, S., Masuyama, T., Lim, Y. J., Hori, M., Kodama, K. and Kamada, T. (1993). Demonstration of functional border zone with myocardial contrast echocardiography in human hearts: simultaneous analysis of myocardial perfusion and wall motion abnormalities. *Circulation* **88,** 447–453.

Needleman, A., Rabinowitz, S. A., Bogen, D. K. and McMahon, T. A. (1983). A finite element model of the infarcted left ventricle. *J. Biomech.* **16,** 45–58.
Olivetti, G., Ricci, R., Beghi, C., Guideri, G. and Anversa, P. (1986). Response of the border zone to myocardial infarction in rats. *Am. J. Pathol.* **125,** 476–483.
Parmley, W. W., Chuck, L. and Kivowitz, C. (1973). In vitro length-tension relations of human ventricular aneurysms. *Am. J. Cardiol.* **32,** 889–894.
Parnell, T. K. (1984). Numerical improvement of asymptotic solutions and nonlinear shell analysis. Ph.D. thesis, Stanford University.
Podszus, W. W. (1992). Mechanics of the heart: a nonlinear laminated shell model of the normal and infarcted left ventricle. Ph.D. thesis, University of Rochester.
Prinzen, F. W., Arts, T., Hoeks, A. P. G. and Reneman, R. S. (1989). Discrepancies between myocardial blood flow and fiber shortening in the ischemic border zone as assessed with video mapping of epicardial deformation. *Eur. J. Physiol.* **415,** 220–229.
Radhakrishnan, S., Ghista, D. N. and Jayaraman, G. (1980). Mechanical analysis of the development of left ventricular aneurysms. *J. Biomech.* **13,** 1031–1039.
Resar, J. R., Livingston, J. Z. and Yin, F. C. P. (1992). In-plane myocardial wall stress is not the primary determinant of coronary systolic flow impediment: a study in the isolated, perfused dog septum. *Circ. Res.* **70,** 583–592.
Sagawa, K., Maughan, L., Suga, H. and Sunagaw, K. (1988). *Cardiac Contraction and the Pressure–Volume Relationship*, Oxford University Press. New York.
Sakai, K., Watanabe, K. and Millard, R. W. (1985). Defining the mechanical border zone: a study in the pig heart. *Am. J. Physiol.* **249,** H88–H94.
Sarnoff, S. J., Braunwald, E., Welch, G. H., Jr, Case, R. B., Stainsby, W. N. and Macruz, R. (1958). Hemodynamic determinants of oxygen consumption of the heart with special reference to the tension-time index. *Am. J. Physiol.* **192,** 148–156.
Schlichter, J., Hellerstein, H. K. and Katz, L. N. (1954). Aneurysm of the heart: a correlative study of one hundred and two proved cases. *Medicine* **33,** 43–86.
Skelton, C. L. and Sonnenblick, E. H. (1974). Myocardial energetics. In *Cardiac Mechanics: Physiological, Clinical, and Mathematical Considerations*, (eds Mirsky, I., Ghista, D. N. and Sandler, H.) Wiley, New York, pp. 113–137.
Streeter, D. D. (1979). Gross morphology and fiber geometry of the heart. In *Handbook of Physiology, Section 2: The Cardiovascular System, Volume I: The Heart*, (eds Berne, R. M., Sperelakis, N. and Geiger, S. R.) American Physiological Society, Bethesda, MD, pp. 61–112.
Taber, L. A. (1987a). On boundary layers in a pressurized Mooney cylinder. *J. Appl. Mech.* **54,** 280–286.
Taber, L. A. (1987b). Large elastic deformation of shear deformable shells of revolution: theory and analysis. *J. Appl. Mech.* **54,** 578–584.
Taber, L. A. (1988). On a theory for large elastic deformation of shells of revolution including torsion and thick-shell effects. *Int. J. Solids Structures* **24,** 973–985.
Taber, L. A. (1989). Comparison of elasticity and shell theory results for large deformation of rubberlike shells. *Int. J. Non-Linear Mech.* **24,** 237–249.
Taber, L. A. (1991a). On a nonlinear theory for muscle shells: II. Application to the active left ventricle. *J. Biomech. Engng* **113,** 63–71.
Taber, L. A. (1991b). On a nonlinear theory for muscle shells: I. Theoretical development. *J. Biomech. Engng* **113,** 56–62.
van Campen, D. H., Huyghe, J. M., Bovendeerd, P. H. M. and Arts, T. (1994). Biomechanics of the heart muscle. *Eur. J. Mech. A/Solids* **13,** 19–41.
van Leuven, S. L., Waldman, L. K., McCulloch, A. D. and Covell, J. W. (1994). Gradients of epicardial strain across the perfusion boundary during acute myocardial ischemia. *Am. J. Physiol.* **267,** H2348–H2362.
Villarreal, F. J., Lew, W. Y. W., Waldman, L. K. and Covell, J. W. (1991). Transmural myocardial deformation in the ischemic canine left ventricle. *Circ. Res.* **68,** 368–381.
Vinson, C. A., Gibson, D. G. and Yettram, A. L. (1979). Analysis of left ventricular behavior in diastole by means of finite element method. *Br. Heart J.* **41,** 60–67.
Weisman, H. F. and Healy, B. (1987). Myocardial infarct expansion, infarct extension, and reinfarction: Pathophysiologic concepts. *Prog. Cardiovasc. Dis.* **30,** 73–110.
Whittaker, P., Boughner, D. R. and Kloner, R. A. (1991). Role of collagen in acute myocardial infarct expansion. *Circulation* **84,** 2123–2134.
Yin, F. C. P. (1981). Ventricular wall stress. *Circ. Res.* **49,** 829–842.
Yin, F. C. P. (1985). Applications of finite-element method to ventricular mechanics. *CRC Crit. Rev. Biomed. Engng* **12,** 311–342.
Zhao, M., Zhang, H., Robinson, T. F., Factor, S. M., Sonnenblick, E. H. and Eng, C. (1987). Profound structural alterations of the extracellular collagen matrix in postischemic dysfunctional ("stunned") but viable myocardium. *J. Am. Coll. Cardiol.* **10,** 1322–1334.

APPENDIX

For axisymmetric deformation of a shell of revolution without surface shear loads, symmetry demands that $\gamma_1 = g_1 = e_{12} = \Gamma_0 = 0$. Then the solution vector

$$\mathbf{y} = [\mathbf{y}_D, \mathbf{y}_4]^T$$

$$\mathbf{y}_D = [(\bar{r}H_2), (\bar{r}M_{22}), r, \phi]^T$$

$$\mathbf{y}_A = [(\bar{r}N_{21}), e_{21}, \lambda_{22}, \kappa_{11}, \kappa_{21}, \kappa_{22}, \gamma_2, g_2]^{\mathrm{T}} \tag{A1}$$

is determined by solving the following 12 equations:

$$\begin{aligned}
(\bar{r}H_2)' &= N_{11} + \frac{e_{21}}{r}(\bar{r}N_{21}) - \bar{r}p_H \\
(\bar{r}M_{22})' &= M_{11}\cos\phi + \frac{\bar{r}e_{21}}{r}M_{21}\cos\phi + (\bar{r}H_2)(\lambda_{22}\sin\phi - \gamma_2\cos\phi) \\
&\quad - \frac{pr^2}{2}\left[1 - \frac{\bar{h}\bar{r}}{r^2\lambda_{22}}\right]^2(\lambda_{22}\cos\phi + \gamma_2\sin\phi) \\
r' &= \lambda_{22}\cos\phi + \gamma_2\sin\phi \\
\phi' &= r\lambda_{22}(\kappa_{22} + \lambda_{22}\bar{\phi}')/\bar{r} \\
0 &= (\bar{r}N_{21})r + \bar{r}M_{21}\sin\phi \\
0 &= \bar{r}^2 r\lambda_{22}\kappa_{11} - \bar{r}^2\sin\phi + r^2\lambda_{22}\sin\bar{\phi} \\
0 &= r^2\lambda_{22}\kappa_{21} - e_{21}\bar{r}\sin\phi + r^2\lambda_{22}e_{21}\bar{\phi}' \\
0 &= \bar{r}^2 S_2 - r\lambda_{22}(\bar{r}H_2)(\lambda_{22}\sin\phi - \gamma_2\cos\phi) \\
&\quad + \frac{pr^3}{2}\lambda_{22}\left[1 - \frac{\bar{h}\bar{r}}{r^2\lambda_{22}}\right]^2(\lambda_{22}\cos\phi + \gamma_2\sin\phi) \\
0 &= (\bar{r}H_2)\cos\phi + \frac{pr^2}{2}\left[1 - \frac{\bar{h}\bar{r}}{r^2\lambda_{22}}\right]^2\sin\phi - \bar{r}N_{22} \\
0 &= (\bar{r}H_2)\sin\phi - \frac{pr^2}{2}\left[1 - \frac{\bar{h}\bar{r}}{r^2\lambda_{22}}\right]^2\cos\phi - \bar{r}Q_2 \\
0 &= \bar{r}\frac{\partial w}{e_{21}} - (\bar{r}N_{21}) \\
0 &= \frac{\bar{r}^2}{r\lambda_{22}}\frac{\partial w}{\partial\kappa_{22}} - (\bar{r}M_{22})
\end{aligned} \tag{A2}$$

where

$$\begin{aligned}
N_{11} &= \bar{r}\frac{\partial w}{\partial r}, \quad N_{22} = \frac{\partial w}{\partial\lambda_{22}} \\
Q_2 &= b\frac{\partial w}{\partial\gamma_2}, \quad S_2 = b\frac{\partial w}{g_2} \\
M_{11} &= \frac{\bar{r}}{r\lambda_{22}}\frac{\partial w}{\partial\kappa_{11}}, \quad M_{21} = \frac{\bar{r}}{r\lambda_{22}}\frac{\partial w}{\partial\kappa_{21}}.
\end{aligned} \tag{A3}$$

In the first equation,

$$p_H = \frac{pr\lambda_{22}}{\bar{r}}\left[1 - \frac{\bar{h}}{r}\left(\kappa_{11}\bar{r} + \frac{r\sin\bar{\phi}}{\bar{r}}\right)\right]\left[1 - \frac{\bar{h}}{\lambda_{22}}(\kappa_{22} + \lambda_{22}\bar{\phi}')\right]\sin(\phi - \Gamma_s) \tag{A4}$$

where

$$\Gamma_s = \tan^{-1}(\gamma_2/\lambda_{22}). \tag{A5}$$

Once $\mathbf{y}$ is obtained, the quantities, z, Ω, ω, λ_{11}, λ_{33}, N_{12}, M_{12}, Q_1, S_1, S_3, H_1, V_1 and V_2 are computed from

$$\begin{aligned}
z' &= \lambda_{22}\sin\phi - \gamma_2\cos\phi \\
\Omega' &= \omega' = e_{21}/r \\
\lambda_{11} &= r/\bar{r} \\
\lambda_{33} &= \bar{r}/(r\lambda_{22}) \\
N_{12} &= \left[\frac{\partial w}{\partial e_{12}}\right]_{e_{12}=0}
\end{aligned}$$

$$M_{12} = \frac{[(\bar{r}(\lambda_{22}(\bar{r}N_{21}) - rN_{12} - e_{21}\bar{r}N_{22})(r\lambda_{22})^{-1} - (\kappa_{21} + e_{21}\bar{\phi}')(\bar{r}M_{22}) + (\kappa_{22} + \lambda_{22}\bar{\phi}')\bar{r}M_{21}]}{\left(\kappa_{11}\bar{r} + \frac{r\sin\bar{\phi}}{\bar{r}}\right)}$$

$$Q_1 = \frac{1}{r}\left[(\bar{r}M_{21})' + M_{12}\cos\phi + \frac{e_{21}}{r}(\bar{r}M_{22})\cos\phi - e_{21}\bar{r}Q_2 + \gamma_2(\bar{r}N_{21})\right]$$

$$S_1 = r\lambda_{22}[rQ_1 - \gamma_2(\bar{r}N_{21}) + e_{21}\bar{r}Q_2]/\bar{r}^2$$

$$S_2 = -\frac{r^2\lambda_{22}^2}{\bar{r}^3}\left[\left(\kappa_{11}\bar{r} + \frac{r\sin\bar{\phi}}{\bar{r}}\right)M_{11} + (\kappa_{21} + e_{21}\bar{\phi}')\bar{r}M_{21} + (\kappa_{22} + \lambda_{22}\bar{\phi}')(\bar{r}M_{22})\right]$$

$$H_1 = N_{12}\cos\phi - Q_1\sin\phi$$

$$V_1 = N_{12}\sin\phi \quad Q_1\cos\phi$$

$$V_2 = \frac{pr^2}{2\bar{r}}\left[1 - \frac{\bar{h}\bar{r}}{r^2\lambda_{22}}\right]^2. \tag{A6}$$